Recent Advances Wind-Assisted Ship and Yacht Sail Aerodynamics

Jean-Baptiste R. G. Souppez
Aston University, UK, j.souppez@aston.ac.uk

Abstract. Wind-assisted ships and racing yachts employ highly cambered sections to maximise performance. However, their complex aerodynamics governed by large regions of flow separation remain to be fully understood. Recently, particle image velocimetry (PIV), performed in water tunnels, has been suggested as a novel experimental technique, provided fundamental spatial and temporal resolution limitations are overcome. Consequently, force measurements and flow visualisation were undertaken on 2D circular arcs, representative of a wind-assisted ship wing, and 3D downwind yacht sails, namely symmetric spinnakers, to ascertain the viability of this experimental approach. The results show that (i) a linear blockage correction can be devised; (ii) a blockage-independent critical Reynolds number and critical angle of attack exist; and (iii) a force crisis occurs because of the suppressed relaminarization of the boundary layer downstream of the leading-edge separation bubble. As such, spatial and temporal limitations can be overcome, yielding novel insights into sail aerodynamics, with PIV in water tunnels shown to be a pertinent methodology for experimental flow visualisation. These findings provide new insights into the aerodynamics of wind-assisted ships and yachts and may contribute to improving their performance by design.

Keywords: aerodynamics, wind-assisted ship propulsion, downwind yacht sails, spinnaker, PIV.

NOMENCLATURE

a	Linear regression coefficient [-]
A	Area [m^2]
A_F	Frontal Area [m^2]
A_R	Aspect ratio [-]
A_S	Sectional Area [m^2]
c	Chord [m]
$\bar{c}$	Average chord [m]
C_D	Drag coefficient [-]
C_{DB}	Drag coefficient with blockage [-]
C_L	Lift coefficient [-]
C_{LB}	Lift coefficient with blockage [-]
d	Sidewall distance [m]
D	Drag [N]
K	Relaminarisation parameter [-]
L	Lift [N]
Re	Reynolds number [-]
s	Span [m]
t	Thickness [m]
u	streamwise velocity [m/s]
$\boldsymbol{u}$	Flow velocity vector [m/s]
u'	Streamwise fluctuations [m/s]
u_∞	Flow speed [m/s]
v'	Streamnormal velocity fluctuations [m/s]
w'	Crossflow velocity fluctuations [m/s]
x	Streamwise coordinate [m]
y	Streamnormal coordinate [m]
y_c	Camber [m]
z	Spanwise coordinate [m]
α	Angle of attack [°]
β_t	True wind angle [°]
η	Rotation angle [°]
κ	Turbulent kinetic energy [m^2/s^2]
ν	Kinematic viscosity [m^2/s]
ρ	Density [kg/m^3]
2D	Two-dimensional
3D	Three-dimensional
CFD	Computational Fluid Dynamics
ESDU	Engineering Sciences Data Unit
ITTC	International Towing Tank Conference
LESB	Leading-Edge Separation Bubble
ORC	Offshore Racing Congress
PIV	Particle Image Velocimetry
TT	Towing tank
WT	Water tunnel

1. INTRODUCTION

The aerodynamics of yacht sails have been thoroughly detailed in the reviews of Larsson (1990), Milgram (1998), Viola (2013) and Souppez et al. (2019), and underpins developments in wind-assisted ship propulsion (Khan et al., 2021). Force measurements have been undertaken in wind tunnels for both wind-assisted ships (Bordogna et al., 2018; Zhang et al., 2021; Banks et al.,2021; Kume et al., 2022) and yacht sails (Fossati et al., 2006; Viola and Flay, 2009; Bot et al., 2014; Magnander and Larsson, 2023), and compared to full-scale measurements (Viola and Flay, 2011). However, quantitative flow visualisation to validate Computational Fluid Dynamics (CFD) remains lacking at model scale (Gauvin and Banks, 2020; Giovannetti et al., 2022), and is impractical at full scale (Souppez and Viola, 2023). This is particularly crucial for highly-cambered geometries, such as cambered and crescent wings (Zeng et al., 2023; Zhu et al., 2023) for wind-assisted ship propulsion, and downwind yacht sails (Arredondo-Galeana et al., 2023; Souppez and Viola, 2024) for sailing yachts. Indeed, these are characterised by large regions of separated flow, which are not reliably analysed with CFD (Hedges et al., 1996).

Quantitative flow visualisation using Particle Image Velocimetry (PIV) could lead to wind-assisted ship and yacht sail aerodynamics breakthroughs. However, limitations are associated with using PIV in wind tunnels (Raffel et al., 2018; Souppez, 2024). Using smoke particles to seed the flow leads to poor light reflection and particle illumination. Consequently, high-power (and therefore high-cost) lasers are needed, which results in light reflection and restricts flow visualisation. Moreover, the dissipation of the smoke in the wind tunnel causes an inconsistent particle density, increasing uncertainty and difficulty reproducing experimental conditions (Gauvin and Banks, 2020; Giovannetti et al., 2022). This contrasts with underwater PIV, which employs highly reflective silver-coated hollow glass spheres, leading to lower power and more affordable lasers and alleviating reflection issues. Furthermore, the particle density is maintained and reproducible. PIV is, therefore, best undertaken in water rather than air.

Consequently, conducting PIV measurements in water tunnels rather than wind tunnels could be a promising experimental methodology for quantitative flow visualisation. However, this requires a high spatial and temporal resolution, only achieved by increasing the model size and decreasing the stream velocity, respectively, leading to two challenges to be overcome:

(1) Large model sizes yield significant blockage ratios, defined as the ratio of the frontal area of the geometry to the tunnel's cross-sectional area, increasing the flow speed around the geometry compared to the free-stream velocity, causing an increase in force coefficients. Lasher et al. (2005) recommended a blockage ratio below 0.05 for highly cambered sails, but recent PIV measurements have been conducted at much higher blockage ratios (Arredondo-Galeana, 2019; Bot, 2020; Arredondo-Galeana et al., 2023, Souppez and Viola, 2024), which are not covered in established blockage corrections (Pope and Harper, 1966; ESDU, 1995; ESDU, 1998). Whether a suitable blockage correction can be established remains to be ascertained.
(2) A low stream velocity results in a low chord-based Reynolds number Re, of the order of 10^4 for water tunnels (Arredondo, 2019; Arredondo-Galeana et al., 2023), compared 10^5 for wind tunnels (Viola and Flay, 2009; Bot et al., 2014) and 10^6 (Collie, 2006; Braun et al., 2016) for full-scale. Therefore, the minimum Reynolds number for experimental testing to yield accurate full-scale results must be quantified.

This paper details the recent advances in the water tunnel testing of wind-assisted ship and yacht sails to obtain force coefficients and quantitative flow fields. Specifically, whether the limitations associated with high spatial and temporal resolution can be overcome will be tackled by investigating a two-dimensional (2D) circular arc representing rigid wings such as DynaRigs and a three-dimensional (3D) downwind yacht sail, i.e. a spinnaker. The remainder of the paper is structured as follows. First, Section 2 introduces the experimental methodology. Then, Section 3 presents the results for both the 2D and 3D geometries. Finally, Section 4 summarises the main findings.

2. METHODOLOGY

2.1 Geometries

Two rigid geometries were investigated, as depicted and Figure 1(a) and Figure 1(b), respectively, with their geometrical characteristics detailed in Table 1; these are:

(1) A 2D circular arc relevant to wind-assisted ships (Bordogna et al., 2018; Zeng et al., 2023; Atkinson and Binns, 2018; Zhu et al., 2022), with a camber-to-chord ratio $y_c/c = 0.2232$, similar to that of Collie (2006), Velychko (2014), Bot et al. (2016), Flay et al. (2017), Bot (2020), and Souppez and Viola (2022). Three carbon fibre arcs were manufactured, with chord lengths $c\ = 100$ mm, 150 mm and 200 mm, and tested at $53\,530\ \leq Re\ \leq 218\,000$.
(2) A 3D sail based on the spinnaker design by Braun et al. (2016). Three spinnakers were 3D printed, with average chord lengths $\bar{c}\ = 85.94$ mm, 107.42 mm and 128.90 mm, and tested at $5\,870\ \leq Re \leq 61\,870$.

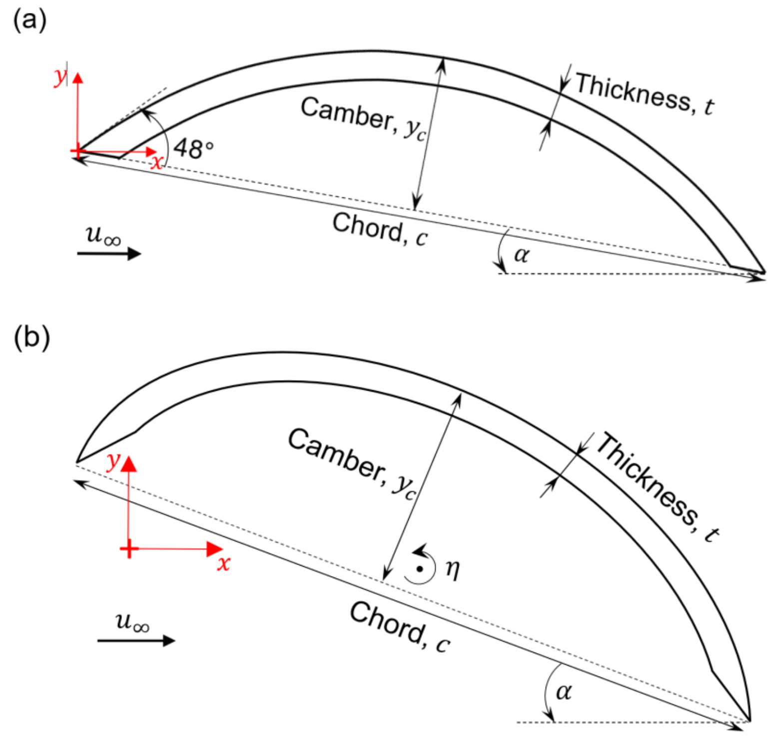

Figure 1. (a) 2D circular arc and (b) midspan section through the 3D sail, where α is the angle of attack, and η is the rotation angle of the sail from its intended operating angle (Braun et al., 2016).

Table 1. Geometrical characteristics of the 2D circular arcs and 3D sails.

Geometry	2D Circular Arcs			3D Sails		
Chord, c [mm] or average chord $\bar{c}$ [mm]	100	150	200	85.94	107.42	128.90
Span, s [mm]	370	370	370	130	162.5	195
Aspect ratio, $A_R = s^2/A$ [-]	3.70	2.47	1.85	1.51	1.51	1.51
Thickness, t [mm]	1.80	1.80	1.80	2.00	2.50	3.00
Thickness-to-chord ratio t/c [-]	0.018	0.012	0.009	0.023	0.023	0.023

2.2 Experimental Setups

Force measurements were conducted in both a 60 m towing tank (TT) (Dewavrin and Souppez, 2018) and an 8 m water tunnel (WT) (Robinson et al., 2015), while PIV was undertaken solely in the water tunnel.

In the towing tank, adjustable sidewalls with a spacing $d = 340$ mm, 550 mm and 1180 mm, as shown in Figure 2(a), are employed on either side of the circular arcs to vary the blockage ratio and, therefore, investigate its effects. Without sidewalls, the towing tank has a width of 3700 mm, and thus blockage is negligible. For the sail, blockage is investigated in the water tunnel by varying the sail's size. In the water tunnel, for PIV measurements, the laser sheet is shown at the suction side of the geometries; see the example of the circular arc in Figure 2(b).

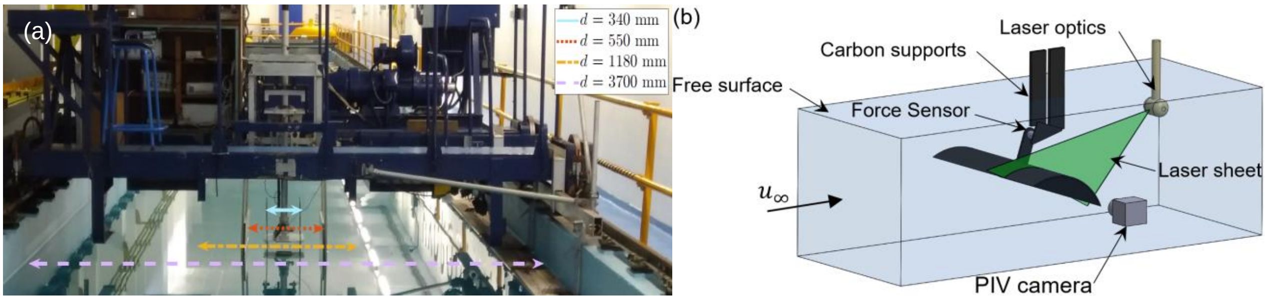

Figure 2. (a) 2D circular arc in the towing tank with sidewall locations, and (b) schematics of the PIV setup in the water tunnel.

2.3 Force and PIV Measurements

Forces are recorded for at least 6 s in the towing tank and 60 s in the water tunnel at a 1 kHz frequency. From the measured lift L and drag D, the lift and drag coefficients are, respectively, given as $C_L = 2L/\rho A u_\infty^2$ and $C_D = 2D/\rho A u_\infty^2$, where ρ is the water density, A is the area, and u_∞ is the flow speed. The uncertainty was computed following the ITTC (2014) methodology and will be presented as vertical error bars in Section 4.

PIV measurements were performed using a 200 mJ Nd:YAG pulsed laser at a 532 nm wavelength, illuminating silver-coated hollow glass spheres. The PIV images were processed using one initial 96 px by 96 px pass with a 50% overlap before three 32 px by 32 px passes with a 75% overlap. As such, a velocity vector is ascertained for an 8 px by 8 px window. The uncertainty based on Corkery et al. (2018) never exceeded ±0.0285u_∞.

3. RESULTS

3.1 Blockage

While blockage effects may be neglected for blockage ratios $A_F/A_S < 0.05$ (Pope and Harper, 1966), the larger model size employed for PIV yield values of A_F/A_S over this range, namely 0.2477 for the circular arc and 0.094 for the sail investigated in this work. However, blockage corrections for lift-generating bodies with significant training-edge separation, such as highly-cambered plates and wings, do not exist (ESDU, 1995; ESDU, 1998). Consequently, the ratio of force coefficients without and with blockage denoted C_L/C_{LB} and C_D/C_{DB} for the lift and drag, respectively, are quantified. These are presented in Figure 3 for increasing blockage ratios, achieved with sidewalls for the circular arc in the towing tank ($A_F/A_S \leq 0.2477$), see Figure 3(a), and different size model sails in the water tunnel ($A_F/A_S \leq 0.094$), see Figure 3(b).

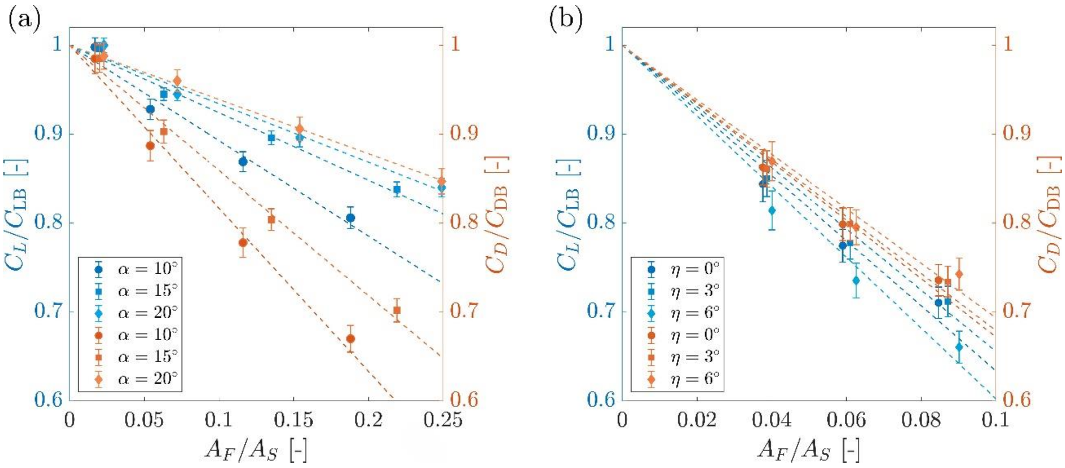

Figure 3. Effect of blockage ratio A_F/A_S for (a) the 2D circular arc and (b) the 3D sail.

For both geometries, linear trends within the bounds of the uncertainty are evidenced. Indeed, as A_F/A_S tends towards 0, C_L/C_{LB} and C_D/C_{DB} tend toward 1. Consequently, a blockage correction equation of the form $C_L/C_{\mathrm{LB}} = a\, A_F/A_S + 1$ for the lift, and $C_D/C_{\mathrm{DB}} = a\, A_F/A_S + 1$ for the drag can be devised, where the linear regression coefficient a is ascertained experimentally, as presented in this work, and enables to correct force coefficients for the effects of blockage. The accuracy of the correction will be demonstrated in the following section.

3.2 Force Crisis

The existence of a drag crisis on circular cylinders is well established (Bloor, 1964) and is characterised by a step decrease in C_D with Re. For the highly-cambered geometries under study, a force crisis occurs (Bot et al., 2016), which consists of a simultaneous step increase in C_L with α, see Figure 4(a), and a step decrease in C_D with α, see Figure 4(b).

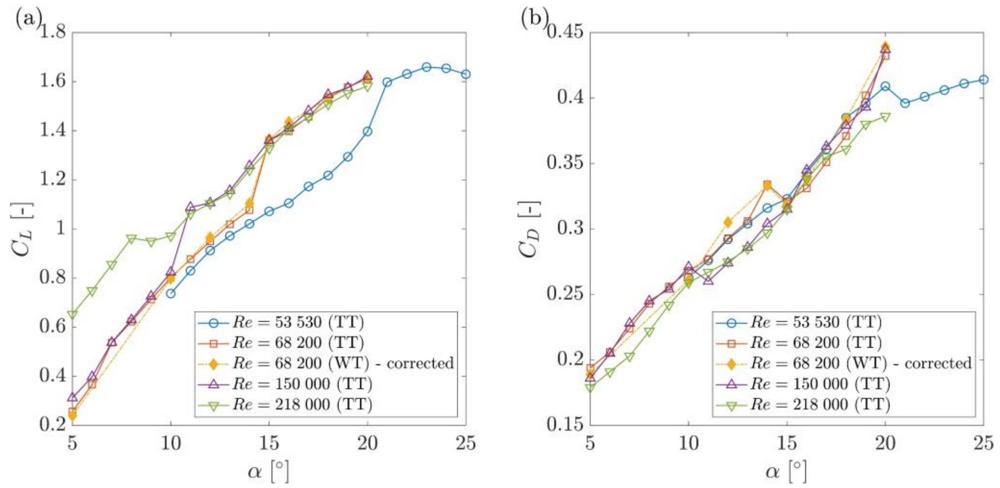

Figure 4. (a) Lift and (b) drag coefficients for the 2D circular arc at $53\,530 \leq Re \leq 218\,000$.

There is no visible force crisis for the 2D circular arc at $Re = 218\,000$ for $5° \leq \alpha \leq 25°$ because, as shown by Bot et al. (2016), the force crisis occurs at $\alpha = 0°$ for $Re = 218\,000$. At $Re = 68\,200$ and $Re = 53\,530$, the force crisis is consistent with those identified by Bot (2020) and Velychko (2014), respectively, on an identical geometry. Note that, at $Re = 68\,200$, the results from the towing tank (no blockage) and the water tunnel (corrected for blockage, as detailed in Section 3.1), yield an excellent agreement, demonstrating the accuracy of the present blockage correction. Therefore, it can also be concluded that the force crisis is independent of the blockage ratio.

The force crisis may be triggered by either an increase in Re, or α. Figure 5(a) shows the variations of C_L and C_D with Re at $\alpha = 11°$, with the force crisis occurring for $142\,000 \leq Re \leq 146\,000$. On the other hand, Figure 5(b) depicts C_L and C_D against α at $Re = 150\,000$, with the force crisis happening for $10° \leq \alpha \leq 11°$.

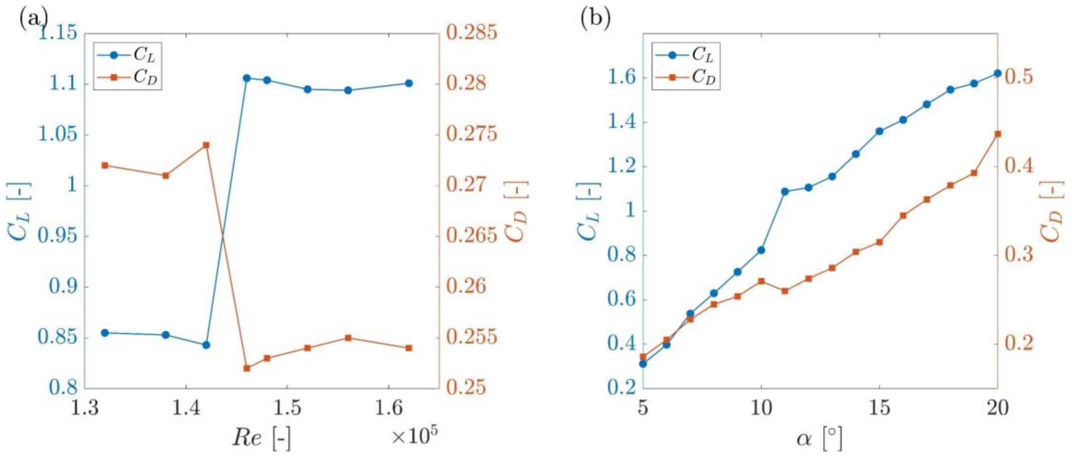

Figure 5. Force crisis for the 2D circular arc versus (a) Re at $\alpha = 11°$, and (b) α at $Re = 68\,200$.

A force crisis is also evidenced by the 3D sail. Because soft sails require a stagnation point on the leading edge or on the pressure side to inflate without inflection, and given that the force crisis for such sails occurs at angles that would not be encountered in realistic sailing conditions (Souppez, 2024), the results focus on the force crisis occurring due to an increase in Re. This is most relevant to the research question tackled in this work, namely whether accurate full-scale measurements can be undertaken at very low Re (circa 10^4).

Figure 6(a) and Figure 6(b) present the lift and drag coefficients, respectively, versus Re. Results are shown for 3 ranges of blockage ratios corresponding to the 3 sails investigated, together with the resulting coefficients extrapolated for $A_F/A_S = 0$ using the linear regression detailed in Section 3.1. For both the lift and drag, the force crisis occurs at $Re = 22\,940$. Contrarily to the 2D circular arc, the force crisis on the 3D sail shows a step increase in C_D with Re. This arises from the induced drag, proportional to the lift squared, absent on 2D geometries but present for the 3D sail.

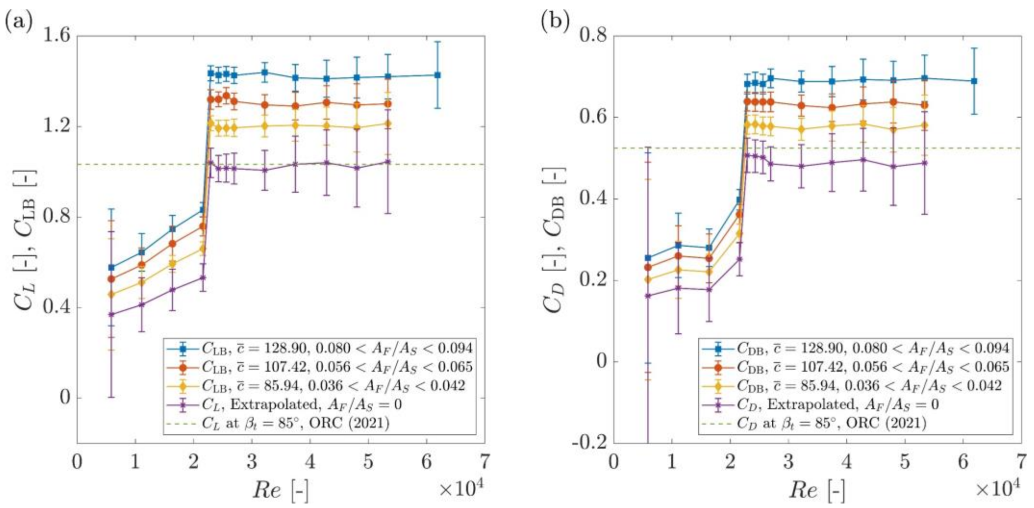

Figure 6. (a) Lift and (b) drag crisis versus for the 3D sail at $\eta = 0°$.

The extrapolated coefficients yield a good agreement with the expected full-scale force coefficients, as defined by the Offshore Racing Congress (ORC), at a true wind angle $\beta_t = 85°$, which corresponds to $\eta = 0°$ (Braun et al., 2016). This further emphasises the accuracy of the blockage correction and the Reynolds-independent nature of the force crisis. Notably, it reveals that force coefficients in line with full-scale ones can be achieved, even at low Re, provided the force crisis occurs. The Re at which the force crisis happens is termed critical Re. While the precise value will depend on the angle of attack of the sail and its geometry, the value of $Re = 22\,940$ is significant because it exceeds that of all previous PIV tests undertaken in water tunnels on such 3D sails (Arredondo-Galeana, 2019; Arredondo-Galeana et al., 2023).

In Section 3.1, the fact that a blockage correction can be experimentally devised for lift-generating, highly-cambered plates and wings demonstrated that the limitations associated with the spatial resolution to undertake PIV in water tunnels can be overcome. In Section 3.2, the force crisis was presented, and the suitability of low Re testing ascertained, provided critical Re or α are exceeded. This ensures that the temporal resolution limitations of water tunnel experiments can also be overcome. Therefore, the proposed experimental methodology is pertinent. Moreover, novel insights can be gained from the applications of PIV, which may contribute to understanding the origin of the force crisis. This is investigated in Section 3.3.

3.3 Flow Visualisation

The flow fields of the suction side of the 2D circular arc at $Re = 68\,200$ are presented in Figure 7, for $\alpha = 12°$, $13°$ and $14°$, i.e. before the force crisis, as well as $\alpha = 15°$, $16°$ and $17°$, once the force crisis has occurred. In addition to the step change in force coefficient evidenced in Section 3.2, there is a reduction of the wake size and downstream shift of the separation point after the force crisis, which could be due to the laminar-to-turbulent transition of the boundary layer.

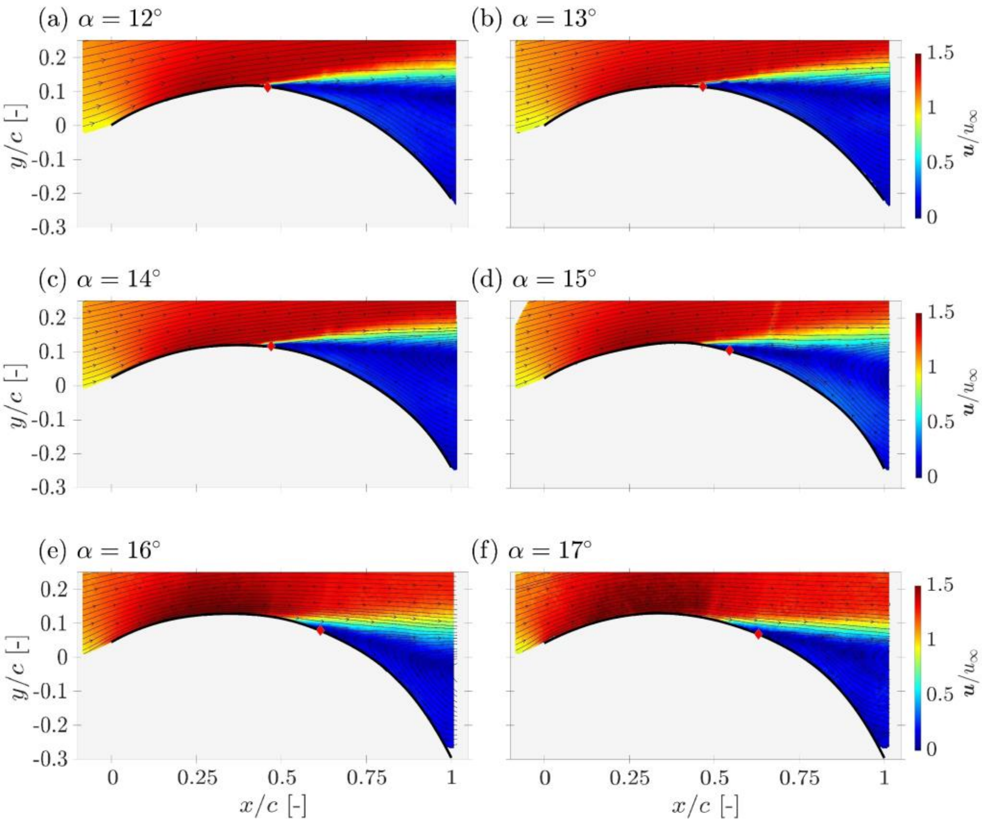

Figure 7. Streamlines and contours of nondimensional flow velocity for the 2D circular arc at $Re = 68\,200$ for angles of attack of (a) 12°, (b) 13°, (c) 14°, (d) 15°, (e) 16° and (f) 17°. Red diamond denotes the separation point.

To investigate this hypothesis, the turbulent kinetic energy κ is computed as

$$\kappa = \frac{\overline{(u')^2} + \overline{(v')^2} + \overline{(w')^2}}{2}, \tag{1}$$

where the variance in flow velocity in the streamwise, streamnormal and crossflow directions are labelled $\overline{(u')^2}$, $\overline{(v')^2}$ and $\overline{(w')^2}$, respectively. Because of the planar PIV setup employed in this work, the $\overline{(w')^2}$ term is neglected. Turbulent flow is considered for $\kappa > 10^{-2}u_\infty$ (Souppez et al., 2022). The results for the 2D circular arc at $Re = 68\,200$ are depicted in Figure 8.

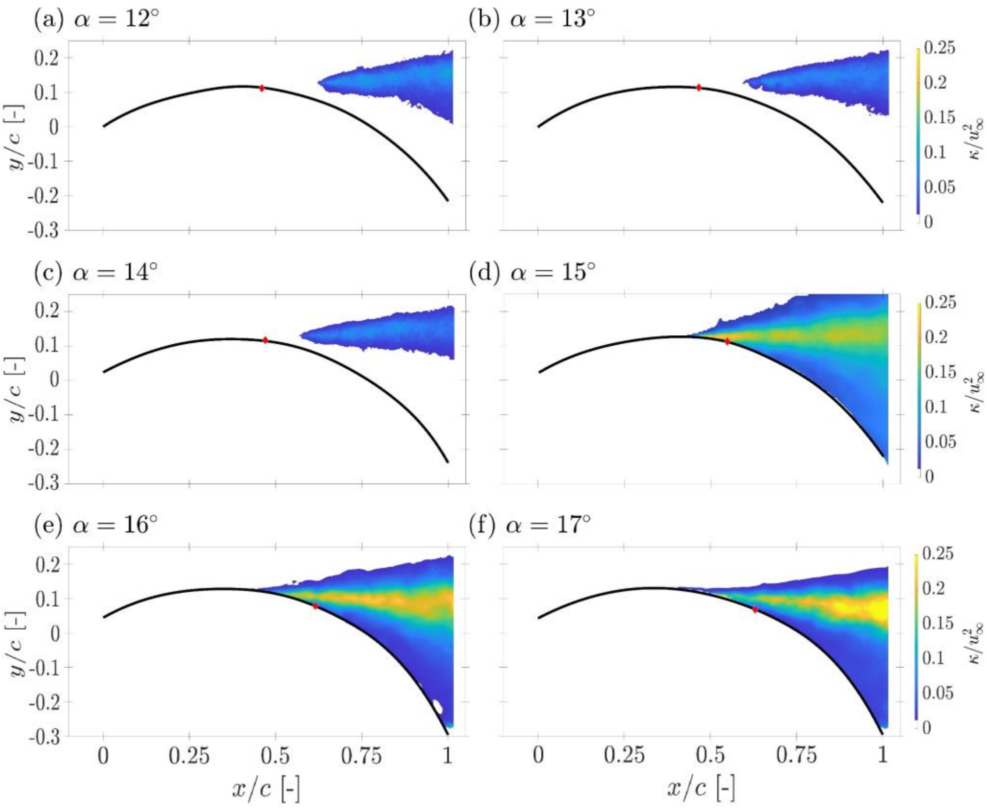

Figure 8. Contours of nondimensional turbulent kinetic energy (plotted for $\kappa > 10^{-2}u_\infty$) for the 2D circular arc at $Re = 68\,200$ for angles of attack (a) 12°, (b) 13°, (c) 14°, (d) 15°, (e) 16° and (f) 17°. Red diamond denotes the separation point.

Prior to the force crisis, transition occurs in the wake, as shown in Figure 8(a)-(c). However, after the force crisis occurs at $14° < \alpha < 15°$, transition is evidenced upstream of the separation points, see Figure 8(d)-(f). The force crisis is, therefore, characterised by a change from laminar to turbulent trailing-edge separation. However, in Figure 8, the PIV resolution is such that the boundary layer is not visible. Consequently, whether the transition occurs immediately at the leading edge, within the Leading-Edge Separation Bubble (LESB), or develops in the boundary layer downstream of the LESB remains to be ascertained.

PIV measurements zoomed-in on the leading edge are undertaken at $\alpha = 13°$ and $\alpha = 16°$, as presented in Figure 9(a) and Figure 9(b), respectively, to capture a change in behaviour prior to ($\alpha = 13°$) and after ($\alpha = 16°$) the force crisis occurring. In both cases, a turbulent LESB is identified thanks to the value of κ. Remarkably, the LESB is followed by a laminar boundary layer at $\alpha = 13°$, but by a turbulent one at $\alpha = 16°$. This suggests relaminarization downstream of the LESB.

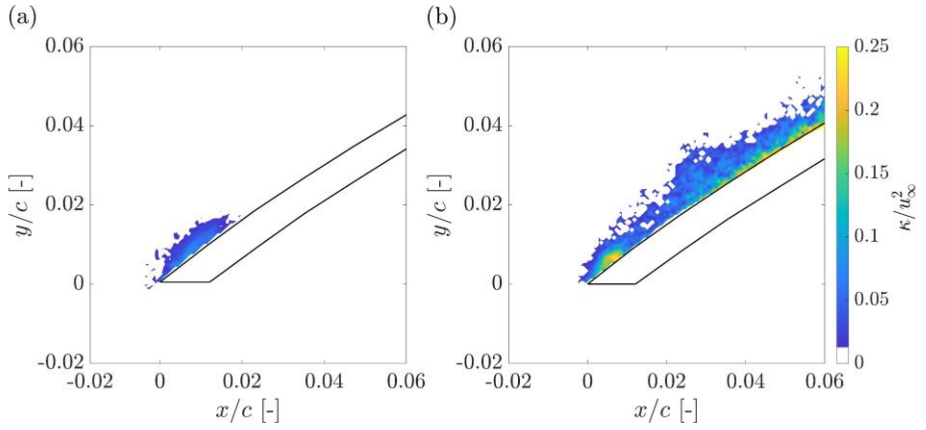

Figure 9. Contours of nondimensional turbulent kinetic energy (plotted for $\kappa > 10^{-2}u_\infty$) for the leading edge of the 2D circular arc at $Re = 68\,200$ for (a) $\alpha = 13°$ and (b) $\alpha = 16°$.

This is indeed the case and is due to the highly accelerated flow (see Figure 7), as verified using the acceleration parameter K (Launder, 1992) and associated relaminarization criterion (Narasimha and Sreenivasan,1979), whereby relaminarization occurs for

$$K = \frac{\nu}{u^2}\frac{\mathrm{d}u}{\mathrm{d}x} \geq 3.5 \times 10^{-6}, \tag{2}$$

where ν is the kinematic viscosity, and u is the local streamwise flow velocity. Therefore, the force crisis on the circular arc originates from the suppressed relaminarization of the boundary layer downstream of the LESB, and not transition in the boundary layer as on circular cylinders (Bloor, 1964). Because the size of the LESB increases for higher α and lower Re, measurements are undertaken at these extremes of the present parameter space, namely $\alpha = 25°$ and $Re = 52\,530$ to better capture the flow features of the LESB, as presented in Figure 10.

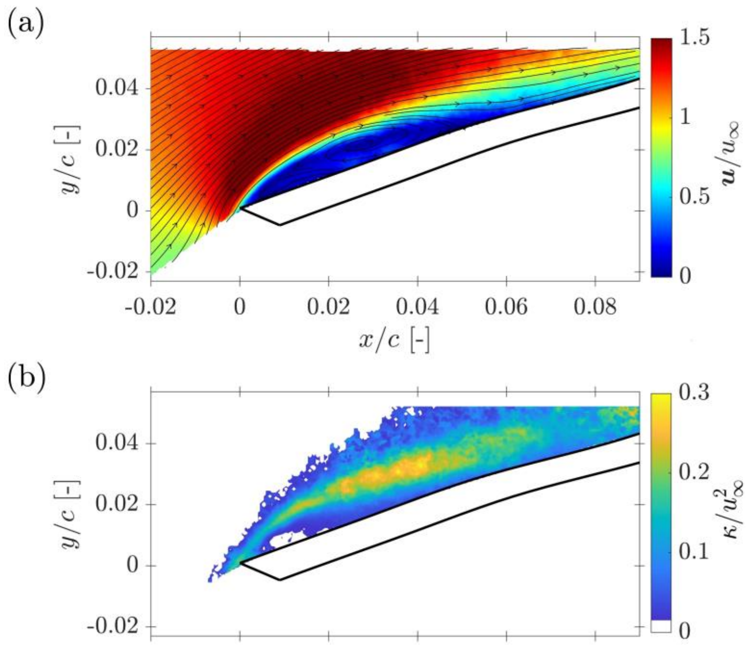

Figure 10. (a) Streamlines and contours of nondimensional flow velocity, and (b) contours of nondimensional turbulent kinetic energy (plotted for $\kappa > 10^{-2}u_\infty$) for the leading edge of the 2D circular arc at $\alpha = 25°$ and $Re = 53\,530$.

Whether the 2D findings, namely that the force crisis is triggered by the suppressed relaminarization of the boundary layer downstream of the LESB, are also valid for 3D sails is ascertained next. This is achieved by comparing the 3D sails at Re below the critical Re, as well as above. Here, $Re = 16\,320$ and $Re = 32\,210$ are considered, with the critical $Re = 22\,940$ (see Section 3.1). The flow fields are captured at 5 spanwise sections z/s, where $z/s = 0$ is the foot of the sail, and $z/s = 1$ is the head of the sail. The spanwise sections considered are 0.88, 0.70, 0.57, 0.37, and 0.05, as shown in Figure 11.

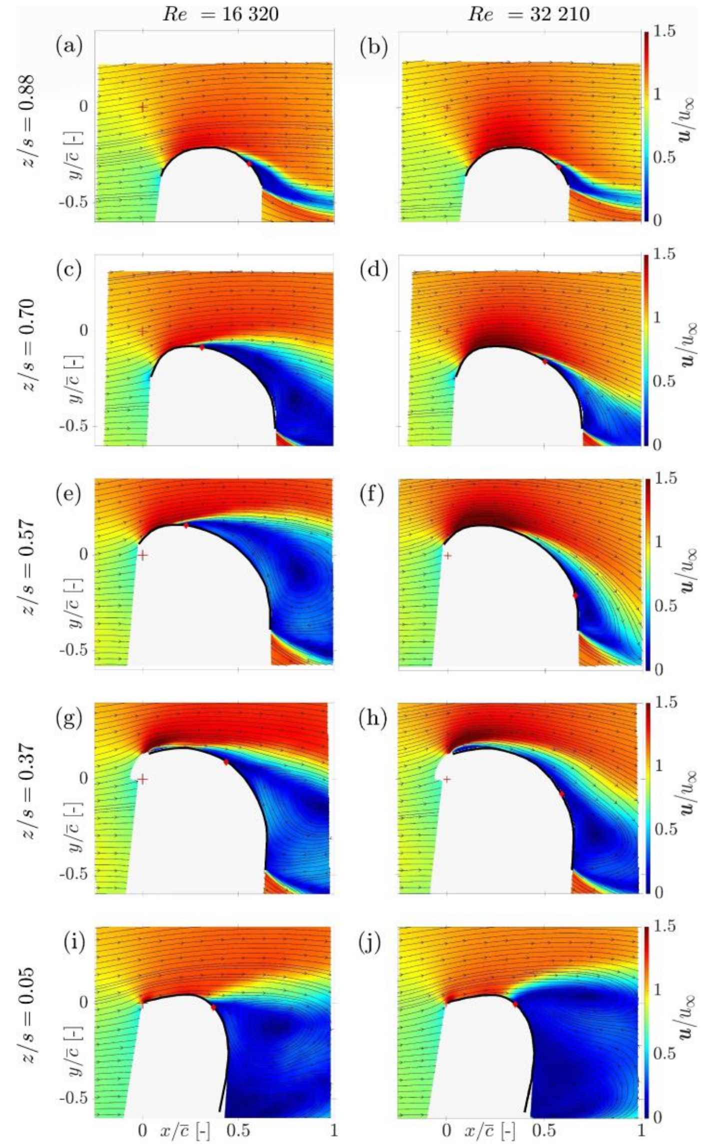

Figure 11. Streamlines and contours of nondimensional flow velocity for the 3D at $\eta = 0°$ for $Re = 16\,320$ (left) and $Re = 32\,210$ (right). Red diamond denotes the separation point.

As for the 2D circular arc, there is a smaller wake and shift of the trailing-edge separation point (red diamond) downstream after the force crisis, except for $z/s = 0.05$ where the flow is governed by the large tip vortex at the foot of the sail. Particular attention is drawn to $z/s = 0.37$ where the LESB is visible in Figure 11(g) and Figure 11(h). Then, the laminar or turbulent nature of the flow is characterised using κ, as presented in Figure 12. For $z/s = 0.88$, 0.70 and 0.57, laminar separation occurs prior to the force crisis, while turbulent separation is evidenced once the critical Re is exceeded. In Figure 11(g) and Figure 11(h), a turbulent LESB is visible, with evidence of relaminarization for the former (below critical Re), but not the latter (above critical Re). Evidence of the force crisis related to the suppressed relaminarization of the boundary layer downstream of the LESB is, therefore, also present for the 3D sail, albeit only at a single spanwise section.

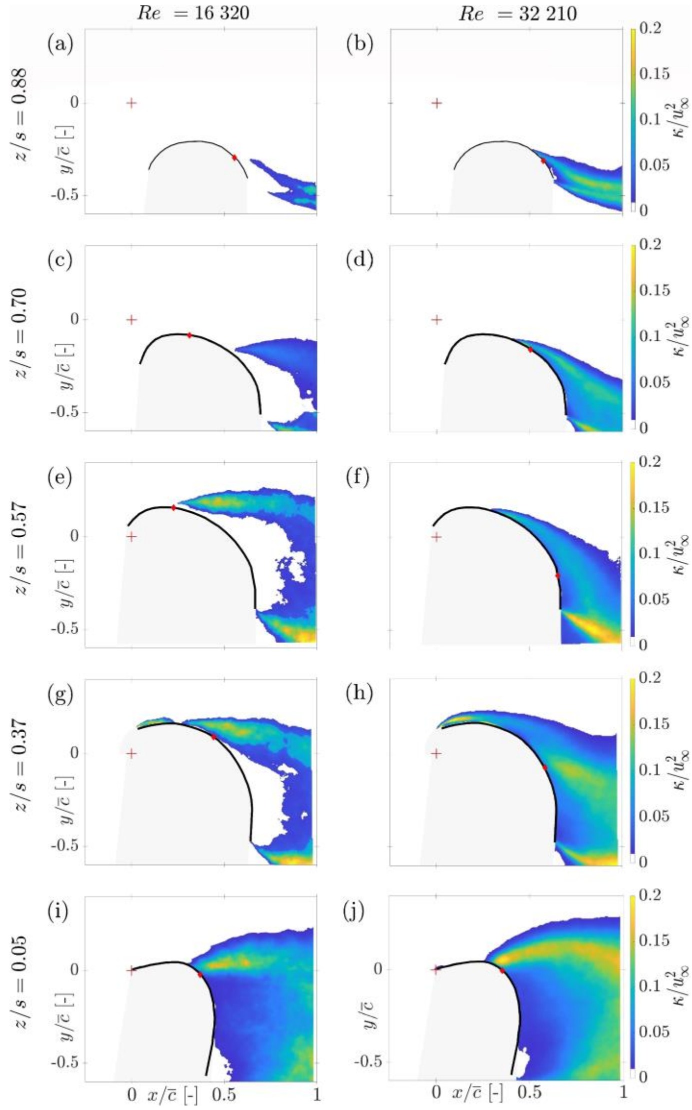

Figure 12. Contours of nondimensional turbulent kinetic energy (plotted for $\kappa > 10^{-2}u_\infty$)for the 3D at $\eta = 0°$ for $Re = 16\ 320$ (left) and $Re = 32\ 210$ (right). Red diamond denotes the separation point.

4. CONCLUSIONS

The aerodynamics of 2D and 3D geometries for wind-assisted ship wings and yacht sails have been investigated, including force measurements and PIV flow visualisation. To facilitate the latter, the experiments were conducted in a water tunnel, thereby leading to spatial and temporal limitations. However, the present work provided a methodology to devise a suitable blockage correction while also identifying the critical conditions, namely Reynolds number and angle of attack, to yield a force crisis. As such, force coefficients identical to that of full scale can be achieved, with PIV in water tunnels shown to be a pertinent methodology for experimental flow visualisation. Indeed, the flow visualisation provided novel insights into the aerodynamics of highly-cambered plates and wings, with the results evidencing that the force crisis occurs because of the suppressed relaminarization of the boundary layer downstream of the leading-edge separation bubble. These findings provide new insights into the aerodynamics of wind-assisted ships wings and yachts sails, for applications ranging from DynaRigs to racing spinnakers, and may contribute to improving their performance by design.

REFERENCES

Arredondo-Galeana, A. (2019). A study of the vortex flows of downwind sails. *PhD Thesis, The University of Edinburgh*.

Arredondo-Galeana, A., Babinsky, H. and Viola, I.M. (2023). Vortex flow of downwind sails. *Flow*, 3: E8. https://doi.org/10.1017/flo.2023.1

Banks, J., Cocard, M. and Jaspe, J., 2021. Assessing the impact of membrane deformations on wing sail performance. Journal of Sailing Technology, 6(01): 73-90. https://doi.org/10.5957/jst/2021.6.1.73

Atkinson, G.M. and Binns, J. (2018). Power profile for segment rigid sail. *Journal of Marine Engineering & Technology*, 17(2): 99-105. https://doi.org/10.1080/20464177.2017.1319997

Bloor, M. S. (1964). The transition to turbulence in the wake of a circular cylinder. *Journal of Fluid Mechanics,* 19(2): 290-304.

Bordogna, G., Keuning, J.A., Huijsmans, R.H.M. and Belloli, M. (2018). Wind-tunnel experiments on the aerodynamic interaction between two rigid sails used for wind-assisted propulsion. *International Shipbuilding Progress*, 65(1): 93-125. http://doi.org/100.3233/ISP-180143

Bot, P. (2020). Force variations related to flow pattern changes around a high-camber thin wing. *AIAA Journal*, 58(5): 1906–1912. https://doi.org/10.2514/1.j058443

Bot, P., Rabaud, M., Thomas, G., Lombardi, A., and Lebret, C. (2016). Sharp transition in the lift force of a fluid flowing past nonsymmetrical obstacles: evidence for a lift crisis in the drag crisis regime. *Physical Review Letters*, 117(23): 234501. https://doi.org/10.1103/PhysRevLett.117.234501

Bot, P., Viola, I. M., Flay, R. G. J., and Brett, J.-S. (2014). Wind-tunnel pressure measurements on model scale rigid downwind sails. *Ocean Engineering*, 90: 84–92. https://doi.org/10.1016/j.oceaneng.2014.07.024

Braun, J., Richelsen, M., and Schreber, M. (2016). Downwind aero moments & forces - phase 2C. *Sailing Yacht Research Foundation*, Warwick, Rhode Island, USA.

Collie S. (2006). Application of computational fluid dynamics of two dimensional downwind sail flows. *PhD thesis, University of Auckland.*

Corkery, S. J., Babinsky, H., and Harvey, J. K. (2018). On the development and early observations from a towing tank-based transverse wing–gust encounter test rig. *Experiments in Fluids*, 59(9), 1–16. http://doi.org/10.1007/s00348-018-2586-0

Dewavrin, J., and Souppez, J. B. R. G. (2018). Experimental Investigation into Modern Hydrofoil-Assisted Monohulls: How Hydrodynamically Efficient are they?. *Transactions of the Royal Institution of Naval Architects Part B: International Journal of Small Craft Technology*, IJSCT223.

ESDU. (1995). *Lift-interference and blockage corrections for two-dimensional subsonic flow in ventilated and closed wind-tunnels*. The Royal Aeronautical Society, London, UK.

ESDU. (1998). *Blockage corrections for bluff bodies in confined flows*. The Royal Aeronautical Society, London, UK.

Flay, R., Piard, A., and Bot, P. (2017). Aerodynamics of a highly cambered circular arc aerofoil: experimental investigations. *4th International Conference on Innovation in High Performance Sailing Yachts*, Lorient, France.

Fossati, F., Muggiasca, S., Viola, I. M. and Zasso, A. (2006). Wind tunnel techniques for investigation and optimization of sailing yachts aerodynamics. *2nd High Performance Yacht Design Conference*, Auckland, New Zealand.

Gauvin, E., and Banks, J. (2020). Measuring the flow-field around flexible downwind sails using particle image velocimetry: A feasibility study into a new experimental approach for the investigation of sailing yacht aerodynamics. *5th International Conference on Innovation in High Performance Sailing Yachts and Sail-Assisted Ship Propulsion*, 27–36.

Giovannetti, L.M., Dhome, U., Malmek, K., Persson, A. and Wielgosz, C. (2022). Multi-wing sails interaction effects. *SNAME Chesapeake Sailing Yacht Symposium*, Annapolis, Maryland, USA.

Hedges, K., Richards, P., and Mallinson, G. (1996). Computer modelling of downwind sails. *Journal of Wind Engineering and Industrial Aerodynamics*, 63(1), 95-110. http://doi.org/10.1016/S0167-6105(96)00071-2

Heng, Z., Yao, H.-D., Thies, R., Ringsberg, J. W., and Ramne, B. (2023) Propulsive performance of a rigid wingsail with crescent-shaped profiles. *Ocean Engineering* 285: 115349. https://doi.org/10.1016/j.oceaneng.2023.115349

ITTC. (2014). ITTC recommended procedures and guidelines: General guideline for uncertainty analysis in resistance test. *ITTC Recommended Procedures and Guidelines*, Copenhagen, Denmark.

Khan, L., Macklin, J., Peck, B., Morton, O. And Souppez, J.-B.R.G. (2021). A review of wind-assisted ship propulsion for sustainable commercial shipping: latest developments and future stakes. *Wind Propulsion Conference, Royal Institution of Naval Architects,* London, UK.

Kume, K., Hamada, T., Kobayashi, H. and Yamanaka, S. (2022). Evaluation of aerodynamic characteristics of a ship with Flettner rotors by wind tunnel tests and RANS-based CFD. *Ocean Engineering*, 254: 111345. https://doi.org/10.1016/j.oceaneng.2022.111345

Larsson, L. (1990). Scientific methods in yacht design. *Annual Review of Fluid Mechanics*, 22(1), 349–385. https://doi.org/10.1146/annurev.fl.22.010190.002025

Lasher, W. C., Sonnenmeier, J. R., Forsman, D. R., and Tomcho, J. (2005). The aerodynamics of symmetric spinnakers. *Journal Of Wind Engineering And Industrial Aerodynamics*, 93(4): 311–337. https://doi.org/10.1016/j.jweia.2005.02.001

Launder, B. E. (1992). Laminarisation of three-dimensional accelerating boundary layers in a curved rectangular-sectioned duct. *International Journal of Heat and Fluid Flow*, 13: 124–131. https://doi.org/10.1115/1.3629738

Milgram, J. H. (1998). Fluid mechanics for sailing vessel design. *Annual Review of Fluid Mechanics*, 30, 613. http://doi.org/10.1146/annurev.fluid.30.1.613

Narasimha, R. and Sreenivasan, K. R. (1979). Relaminarisation of fluid flows. *Advances in Applied Mechanics*, 19: 221–309 (1979). https://doi.org/10.1016/S0065-2156(08)70311-9

ORC, (2021). ORC VPP Documentation. Offshore racing Congress.

Pope, A., and Harper, J. (1966). *Low-speed wind tunnel testing*. New York: Wiley.

Raffel, M., Willert, C.E., Scarano, F., Kähler, C.J., Wereley, S.T. and Kompenhans, J. (2018). *Particle image velocimetry: a practical guide*. Springer, ISBN : 978-3-319-68851-0.

Robinson, A., Ingram, D., Bryden, I., and Bruce, T. (2015). The effect of inlet design on the flow within a combined waves and current flumes, test tank and basins. *Coastal Engineering*, 95, 117–129. https://doi.org/10.1016/j.coastaleng.2014.10.004

Souppez, J.-B. R. G. (2024). Water tunnel testing of highly-cambered plates and wings for downwind yacht sail applications. *PhD Thesis, The University of Edinburgh*. http://dx.doi.org/10.7488/era/4235

Souppez, J.-B. R. G., Arredondo-Galeana, A., and Viola, I. M. (2019). Recent advances in numerical and experimental downwind sail aerodynamics. *Journal of Sailing Technology*, 4(01), 45–65. https://doi.org/10.5957/jst.2019.4.1.45

Souppez, J.-B. R. G., Bot, P., and Viola, I. M. (2022). Turbulent flow around circular arcs. Physics of Fluids, 34, 015121. https://doi.org/10.1063/5.0075875

Souppez, J.-B. R. G., and Viola, I. M. (2022). High-blockage corrections for circular arcs at transitional Reynolds numbers. *Journal of Wind Engineering and Industrial Aerodynamics*, 229, 105139. https://doi.org/10.1016/j.jweia.2022.105139

Souppez, J. B. R. G., and Viola, I. M. (2023). Experimental Force Measurements and Flow Visualisation around Down-wind Yacht Sails. 6th *International Conference on Innovation In High Performance Sailing Yachts and Wind-Assisted Ships,* 221-242.

Souppez, J.-B. R. G., and Viola, I. M. (2024). Water tunnel testing of downwind yacht sails. *Experiments in Fluids,* 65, 2: 1-19. https://doi.org/10.1007/s00348-023-03752-2

Magnander, G. and Larsson, L., 2023. Wind-Tunnel Investigation of the ILCA 7 MKII Sail in Downwind Conditions. *Journal of Sailing Technology*, 8(01): 118-142. https://doi.org/10.5957/jst/2023.8.7.118

Velychko, N. (2014). Study of highly cambered aerofoil using JR3 sensor. *Department of Mechanical Engineering, The University of Auckland.*

Viola, I. M. (2013). Recent advances in sailing yacht aerodynamics. *Applied Mechanics Reviews*, 65(4). http://doi.org/10.1115/1.4024947

Viola, I. M. and Flay, R. G. J. (2009). Force and pressure investigation of modern asymmetric spinnakers. *Transactions of the Royal Institution of Naval Architects Part B: International Journal of Small Craft Technology*, 151(2): 31-40.

Viola, I. M., and Flay, R. G. J (2011). Sail pressures from full-scale, wind-tunnel and numerical investigations. *Ocean Engineering* 38(16): 1733-1743. https://doi.org/10.1016/j.oceaneng.2011.08.001

Zhang, H., Hu, Y. and He, J. (2021). Wind tunnel experiment of multi-mode arc sail device. *Polish Maritime Research*, 28(4): 20-29. https://doi.org/10.2478/pomr-2021-0046

Zeng, Q., Zhang, X., Cai, W. and Zhou, Y. (2023). Wake distortion analysis of a Dynarig and its application in a sail array design. *Ocean Engineering*, 278, p.114341. https://doi.org/10.1016/j.oceaneng.2023.114341